

Porphyrin functionalization of CsPbBr₂/SiO₂ core-shell nanocrystals enhances the stability and efficiency in electroluminescent devices

Jan Wahl, Manuel Engelmayer, Mukunda Mandal, Tassilo Naujoks, Philipp Haizmann, Andre Maier, Heiko Peisert, Denis Andrienko, Wolfgang Brütting, Marcus Scheele

Angaben zur Veröffentlichung / Publication details:

Wahl, Jan, Manuel Engelmayer, Mukunda Mandal, Tassilo Naujoks, Philipp Haizmann, Andre Maier, Heiko Peisert, Denis Andrienko, Wolfgang Brütting, and Marcus Scheele. 2021. "Porphyrin functionalization of CsPbBr₂/SiO₂ core-shell nanocrystals enhances the stability and efficiency in electroluminescent devices." *Advanced Optical Materials* 10 (4): 2101945. <https://doi.org/10.1002/adom.202101945>.

Porphyrin Functionalization of CsPbBr₂/SiO₂ Core–Shell Nanocrystals Enhances the Stability and Efficiency in Electroluminescent Devices

Jan Wahl, Manuel Engelmayer, Mukunda Mandal, Tassilo Naujoks, Philipp Haizmann, Andre Maier, Heiko Peisert, Denis Andrienko,* Wolfgang Brütting,* and Marcus Scheele*

Surface ligand exchange on all-inorganic perovskite nanocrystals of composition CsPbBr₂ reveals improved optoelectronic properties due to strong interactions of the nanocrystal with mono-functionalized porphyrin derivatives. The interaction is verified experimentally with an array of spectroscopic measurements as well as computationally by exploiting density functional theory calculations. The enhanced current efficiency is attributed to a lowering of the charging energy by a factor of 2–3, which is determined by combining electronic and optical measurements on a selection of ligands. The coupled organic–inorganic nanostructures are successfully deployed in a light-emitting device with higher current efficacy and improved charge carrier balance, magnifying the efficiency almost fivefold compared to the native ligand.

significant advances with regards to efficiency.^[1,2] Perovskite nanocrystals (NCs) are particularly promising for realizing LEDs due to their unique properties. Specifically, the large surface area of NCs offers numerous possibilities for functionalization with a variety of surface ligands. Therefore, a major challenge toward advancing nanocrystal-based LEDs is the search for a suitable functionalization. A suitable ligand can modify the NCs, and vice versa, in a variety of ways, which can be exploited to prepare novel materials that fit specific needs. This has previously been shown on well-characterized nanoparticle systems and is providing the foundation of the present work, which focuses on the enhancement of the optoelectronic properties by exchanging the native ligand shell with porphyrin-based ligands.^[3–6] In the case of perovskite nanocrystals, a ligand exchange is inherently difficult due to the instability of the particles against polar environments. However, it holds the potential of improving crucial parameters such as conductivity, stability, and device efficiency.^[1] In practice, this is realized by introducing a ligand with a higher binding affinity to the surface, which can lead to more stable NCs.^[7] Additionally, the electronic coupling between NC and ligand can be adjusted and subsequently used to modify the optoelectronic properties at the interface.^[3,5,8] Following this rationale, we introduce a series of novel surface ligands, i.e., the semiconducting 5-monocarboxyphenyl-10,15,20-triphenylporphyrin and its metalated analogs, in an attempt to improve both stability and current efficiency. Porphyrins have already shown improved efficiency in perovskite-based light harvesting devices as an intermediate layer, which makes them a suitable candidate for functionalized hybrid materials.^[9,10] Here, we investigate how this surface ligand affects key parameters of CsPbBr₂ NC-based LEDs, namely, the current efficacy and turn-on voltage. To this end, we demonstrate how exchange with this porphyrin surface ligand becomes possible without deteriorating the perovskite nanocrystal by stabilizing the surface with a thin silica shell prior to ligand exchange. We show the effects of the porphyrin on the absorption, fluorescence, and electrical transport in macroscopic thin films of the exchanged NCs and find a significant suppression of parasitic ionic transport, an increased crystal phase stability, reduced fluorescence lifetime as well as bright and narrow electroluminescence at 650 nm.

1. Introduction

Lead-halide perovskite-based light-emitting devices (LEDs), both all-inorganic (e.g., CsPbX₃; X = Cl, Br, I) and hybrid (e.g., MAPbX₃; MA = methylammonium) variants, recently made

J. Wahl, P. Haizmann, A. Maier, H. Peisert, M. Scheele
Institute of Theoretical and Physical Chemistry
Eberhard-Karls University of Tübingen
72076 Tübingen, Germany
E-mail: marcus.scheele@uni-tuebingen.de

M. Engelmayer, T. Naujoks, W. Brütting
Institute of Physics
University of Augsburg
86135 Augsburg, Germany
E-mail: bruetting@physik.uni-augsburg.de

M. Mandal, D. Andrienko
Max Planck Institute for Polymer Research
55128 Mainz, Germany
E-mail: denis.andrienko@mpip-mainz.mpg.de

M. Scheele
Center for Light-Matter Interaction, Sensors and Analytics (LISA+)
Eberhard-Karls University of Tübingen
72076 Tübingen, Germany

 The ORCID identification number(s) for the author(s) of this article can be found under <https://doi.org/10.1002/adom.202101945>.

© 2021 The Authors. Advanced Optical Materials published by Wiley-VCH GmbH. This is an open access article under the terms of the Creative Commons Attribution-NonCommercial License, which permits use, distribution and reproduction in any medium, provided the original work is properly cited and is not used for commercial purposes.

DOI: 10.1002/adom.202101945

In LEDs, these CsPbBr₂@SiO_x@porphyrin hybrid NC materials exhibit improved current efficiencies, which we attribute to a reduction of exciton quenching and an improved charge carrier balance.

2. Results and Discussion

2.1. Structure and Core–Shell Synthesis

We find that exchange with ligands bearing polar functional groups on perovskite NCs is inherently difficult. To overcome this, we synthesized a silica shell (SiO_x) around the perovskite core to enhance its stability (details in Figure S3, Supporting Information).^[11] To monitor the particle and superstructure morphology during the preparation process, scanning electron microscopy (SEM) and atomic force microscopy (AFM) measurements were taken before and after the shell growth, which displayed homogeneous, well-defined thin films with a thickness of ≈15–19 nm, corresponding to ≈1 monolayer of NCs. By comparing the images before and after the shell growth, we find an increase of the particle diameter from $d_0 = 8.9 \pm 1.2$ nm to $d_1 = 10.9 \pm 1.4$ nm. This suggests that a silica shell with a thickness of ≈1 nm was synthesized (Figure S1a,b, Supporting Information). These NCs will be referred to as “CsPbBr₂@SiO_x@OAOAm” from here on. Further images, size distributions and spectroscopic analyses are given in Figures S1 and S2 (Supporting Information). The expected improvement in stability is especially beneficial for the functionalization with a polar ligand, like metal-(5-monocarboxyphenyl-10,15,20-triphenylporphyrin) (mMTPP, Figure 1b).

The semiconducting character and interaction as an intermediate layer in perovskite devices predestine this porphyrin as a promising class of surface ligand and was subsequently used to functionalize the SiO_x-coated nanocrystal.^[9,10] After

functionalization with the organic semiconductor, no apparent changes in morphology could be observed as the particles maintained their cubic shape and size (Figure 2b), indicating that the ligand preserves the structural integrity. These NCs will be referred to as “CsPbBr₂@SiO_x@mMTPP” from here on. In the following, all characterization methods were carried out on CsPbBr₂@SiO_x NCs, except the density functional theory (DFT) calculations, which were done without consideration of the shell. However, it is likely that the SiO_x shell may be partially incomplete or contain voids as the exact structure, homogeneity, and coverage are unknown.

2.2. Ligand Exchange

The solution-based ligand exchange with different mMTPP derivatives (Figure 1b) was monitored by nuclear magnetic resonance (NMR) (Figure 1a). Conveniently, a peculiarity of the iodide containing perovskites is the catalysis of amide formation,^[12] which we use here to monitor the exchange. The characteristic amide peak at ≈4.6 ppm experienced a clearly visible upfield shift, which is commonly attributed to a detachment of the native ligand.^[13] Additionally, a downfield shift for the proton peaks in the characteristic porphyrin region (7.5–9 ppm) suggests successful binding of the desired ligand.

Because mMTPP is significantly more polar than oleic acid (OA) and oleylamine (OAm), the surface dipole moment is expected to change upon introducing the novel ligand, hence shifting the absolute energy levels, depending on the strength and orientation of said dipole moment.^[5] Generally, a reduction of the surface dipole, i.e., if it is (partially) lowered by the attached ligand, the energy levels of the NC are shifted to lower energies.^[5] Because mMTPP has a pronounced π -system and an asymmetric functionalization, it provides an intrinsic dipole moment. This dipole is directed contrary to the surface

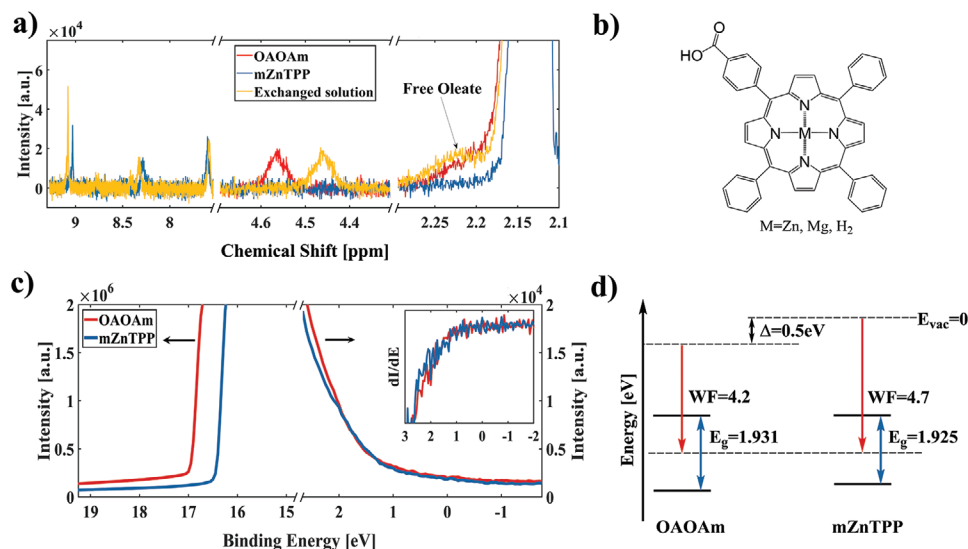


Figure 1. a) NMR analysis of the ligand exchange with mZnTPP. Shown are the regions for the characteristic porphyrin (7.5–9 ppm), amide proton (4.4–4.6 ppm), and the caesium oleate (2.2–2.25 ppm) peaks. b) Structure of the metal-(5-monocarboxyphenyl-10,15,20-triphenylporphyrin) derivatives described throughout this work. c) UPS of thin films before (blue) and after (red) ligand exchange. The inset displays the derivative. d) Corresponding electronic structure of the films, shown are the work functions (red) and band gap energies (blue). The values are referenced against the instrument Fermi level. Overview spectra of the NMR and UPS measurements can be found in Figures S4 and S5 (Supporting Information).

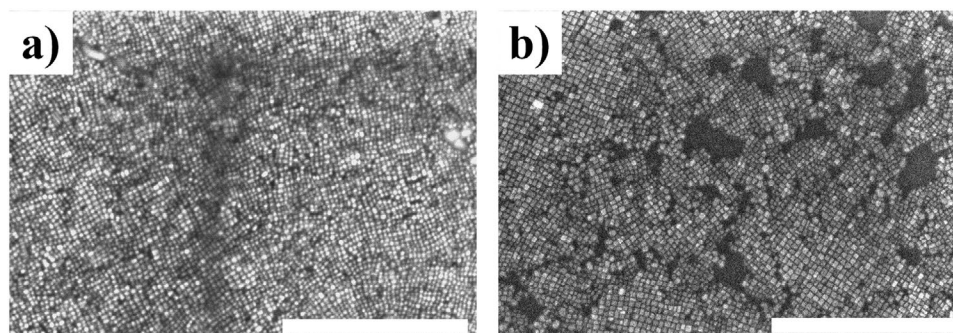


Figure 2. SEM images of CsPbBr₂ nanocrystals showing the preservation of the structural integrity during the preparation and ligand exchange processes. a) Untreated CsPbBr₂ NCs without inorganic shell, and b) after the shell synthesis and ligand exchange with the porphyrin (CsPbBr₂@SiO_x@mZnTPP). Scale bars correspond to 500 nm.

dipole moment of the NCs and is thus able to partially compensate it. We find a shift of the Fermi level by 0.5 eV to lower energies in the case of zinc-(5-monocarboxyphenyl)-10,15,20-triphenylporphyrin (mZnTPP) (Figure 1c,d), confirming the electronic interaction of the NCs and the novel ligand. In both native and porphyrin-functionalized cases, however, the Fermi level remained in the middle of the respective band gap, indicated by the same onset of the valence band maximum (inset of Figure 1c), which can be understood as an indicator for preservation of the valence electronic structure.

2.3. Optical Properties

The native CsPbBr₂@SiO_x@OAOAm sample exhibits the typical spectroscopic features for this composition and a quantum

yield of ≈60%. The absorption spectra (Figure 3a) confirm the preservation of the first excitonic transition from the valence state (1S_v) to the conduction state (1S_c) of the NCs as the onset of the absorption is independent of the amount of ligand added. Nevertheless, increasing the ligand content leads to more pronounced characteristic absorption peaks, namely, the Q-bands of the porphyrin. Strikingly, these bands are shifted to lower energies when compared to an isolated mZnTPP sample. This can be attributed to a pronounced interaction between the particle and ligand since porphyrins are very sensitive towards electronic changes in their periphery.

By comparison with the photoluminescence (PL) spectrum of pure mZnTPP (spectra shown in Figure S6, Supporting Information), we verify that the emission of the mixed solution originates purely from the perovskite NCs. Upon addition of mZnTPP, we observe a redshift in the emission by 6 meV and

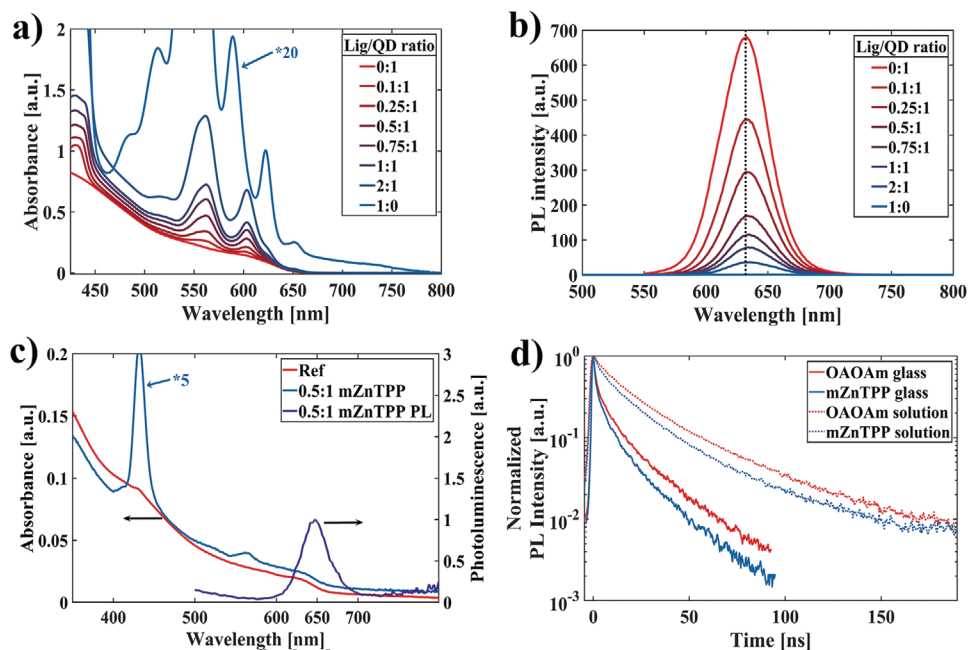


Figure 3. a) UV-vis and b) photoluminescence (PL) in toluene with different stoichiometric amounts of mZnTPP added. c) Solid-state absorption and PL. d) Exciton lifetime measurement of native and exchanged samples in both solution and on a glass substrate.

Table 1. Measured photoluminescence lifetimes (τ_i) of CsPbBrI₂@SiO_x samples on glass and in solution. The values were obtained by fitting the PL decay with a triexponential function. The goodness of the fit is given as the R-squared factor (R^2).

Ligand	Solution				Solid state			
	Lifetime τ_i [ns]			R^2	Lifetime τ_i [ns]			R^2
	τ_1	τ_2	τ_3		τ_1	τ_2	τ_3	
OAOAm	2.89	13.82	39.27	0.99985	1.09	6.59	22.46	0.99971
mZnTPP	2.25	12.93	34.06	0.99983	0.84	4.80	17.34	0.99957

a decrease in quantum yield (QY) as indicated by the reduced emission intensity (Figure 3b). Moreover, fluorescence lifetime measurements display 30% shorter lifetimes after ligand exchange (Table 1), indicating an enhanced interaction between particle and ligand. The redshift in the emission spectra can be explained by a spatial extension of the exciton wavefunction onto the ligand, a changed dielectric environment or a combination of both. Likewise, the shorter fluorescence lifetime can be rationalized as follows: by extending the excitonic wavefunction onto the ligand, the quantum confinement is lowered which results in decreased exciton binding energies.^[14,15] The lowering of the quantum confinement thus destabilizes the exciton, yielding decreased PL lifetimes. This is consistent with the observed behavior in the solid state where the nearest neighbor interaction enhances the said effect, resulting in a bathochromic shift from 635 to 650 nm (Figure 3c) and a further reduction of the lifetime by a factor of 2–3 (Figure 3d and Table 1). Additionally, a separation of excitons can occur in the system, as the conduction state (1S_c) is shifted onto the ligand in the CsPbBrI₂@SiO_x@mZnTPP NCs (Figure 5d). Long-lived excitons can thus be split and are able to recombine nonradiatively on the ligand. Especially porphyrins are known for providing a variety of radiationless transitions.^[16–18] This scenario would also invoke a decrease in PL lifetime and QY.

2.4. Electronic Properties

As perovskites are both electronic and ionic conductors, both transport pathways need to be considered. This can be effectively described by a parallel connection of an electronic (ρ_{el}) and ionic resistance (ρ_{ion})^[19,20]

$$\frac{1}{\rho_{film}} = \frac{1}{\rho_{el}} + \frac{1}{\rho_{ion}} \quad (1)$$

To derive ρ_{el} from Equation (1), the ionic part has to be eliminated. As the ionic contribution behaves like a capacitor, it can be saturated by a potentiostatic measurement, i.e., if a constant voltage over a prolonged period of time is applied. By combining a standard current–voltage curve to obtain the film resistance (ρ_{film}) and the potentiostatic measurement for ρ_{el} , the specific resistances with varying ligand content were analyzed (Figure 4a). The resistance of the system increases dramatically if 0.5 or more equivalents of mZnTPP are added. The most probable reason is a saturation of the NC surface and the allocation of free, excess ligand between the particles. At lower stoichiometric additions, the ratio ρ_{el}/ρ_{ion} decreases, while the overall film resistance stays constant (Figure 4b). To validate

these findings and further explore the conduction mechanism, temperature-dependent conductivity measurements were carried out. The results were fitted using an Arrhenius type nearest neighbor hopping (NNH) model

$$\sigma(T) = \sigma_0 \exp\left\{-\frac{E_A}{k_B T}\right\} \quad (2)$$

with the conductivity σ_0 , Boltzmann's constant k_B , temperature T , and the hopping activation energy E_A . Upon mZnTPP-functionalization, the activation energy in the exchanged system was reduced by over 33% for the electron hopping, whereas the energy for the ion transport did not change significantly (Figure 4c, Table 2, and Figure S7, Supporting Information), which further supports our claim of improved electrical properties of the mZnTPP ligand system.

We note that the temperature-dependent conductivity of the native system cannot be described with a single linear fit, which we tentatively attribute to a phase transition at around 290 K. To verify this assumption, the PL was additionally monitored over the same temperature range (Figure 4d). Two observations were evident, the emission peak shifted to lower energies upon cooling the sample and the full width at half maximum (FWHM) exhibited a maximum at 290 K. The shift arises due to the thermal compression of the lattice and an increased interaction between lead and halides, resulting in a broadening of states at the valence band edge which reduces the size of the band gap, this is consistent with previous reports on perovskites.^[21,22] Further, as the FWHM of the PL signal is phonon-dependent and typically increases with temperature $\text{FWHM} \propto \exp\{E_{LO}/(k_B T)\}^{-1}$, a necessity of the decrease in broadening with higher temperature is a phase transition. Tang et al. have investigated the electron–phonon coupling of different perovskite phases and their temperature dependent behavior.^[22] They found the energy of the longitudinal optical phonon in cubic nanoparticles to be two times larger than in the corresponding orthorhombic counterparts, therefore, a transition from predominantly cubic ($T > 290$ K) to orthorhombic ($T < 290$ K) could explain the decrease of FWHM as observed in Figure 4.^[23,24]

2.5. Charging Energy

To clarify the origin of the altered optoelectronic properties, the dependence of the conductivity on the charging energy (E_C) was considered, which describes the energy required to introduce charges in a nanocrystal. Following the modified Laikhtman–Wolf model, E_C is defined as^[25]

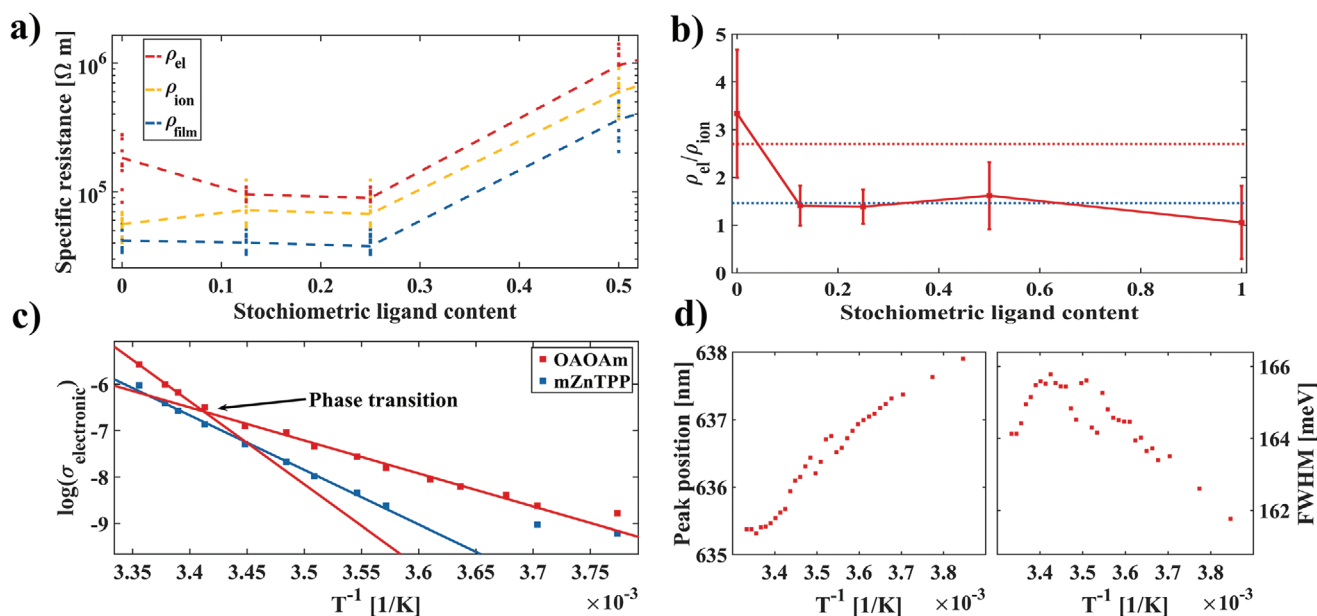


Figure 4. a) Specific resistances of thin films with different ligand compositions. The electronic (red) and ionic (orange) contributions to the overall ohmic resistance (blue) are shown. b) Ratio of electronic and ionic resistance at different stoichiometric values. Dotted lines represent the ratio of electronic and ionic activation energies obtained from temperature dependent conductivity measurements. c) Temperature dependence of the electronic contribution with the corresponding fitting functions. The ionic contribution is given in Figure S7 (Supporting Information). d) Temperature-dependent PL measurements. Position (left) and FWHM (right) of the PL peak in dependence of temperature.

$$E_C = \frac{e^2}{2(C_s + n C_m)} \quad (3)$$

with the elementary charge e , self-capacitance C_s , number of nearest neighbors n , and the mutual capacitance C_m . A more detailed derivation of the components can be found in Section S9 (Supporting Information).

To evaluate the main influence of the charging energy on the charge carrier dynamics, the $\text{CsPbBrI}_2@SiO_x$ NCs were functionalized with mMTPP derivatives. Upon comparing the measured, normalized specific resistance ratios (SRR) with the charging energy E_C of the different systems, it becomes clear that the improvement of the electronic properties follows the same trend as E_C (Figure 5a, suggesting that the charging energy has the main influence. Quantitatively, the charging energy of the exchanged samples, displayed in Figure 5a, is lowered by a factor of $\approx 2.4\text{--}3$ compared to the $\text{CsPbBrI}_2@SiO_x@OAOAm$ NCs (see Table 3). We note that although mMgTPP and mH2TPP showed beneficial electrical properties

Table 2. Results of the Arrhenius type NNH fit of the temperature dependent conductivities. The electronic activation energy (E_A^{el}) and ionic activation energy (E_A^{ion}) were measured. In the case of the native OAOAm ligand shell, the higher temperature fit was used. The ratio of the energies was compared to the measured specific resistance ratio (SRR) as shown in Figure 4b.

	OAOAm	mZnTPP
E_A^{el} [eV]	3.56	2.34
E_A^{ion} [eV]	1.38	1.41
$E_A^{\text{el}}/E_A^{\text{ion}}$	2.57	1.65
$\rho_{\text{el}}/\rho_{\text{ion}}$	3.2	1.5

compared to mZnTPP, such as a better SRR and lower E_C , they were found unsuitable for light emitting devices due to parasitic emission at longer wavelength (Figure 5b).

To probe the effect of the ligand used for surface functionalization on the electronic structure of the NC/ligand hybrid system, density functional calculations were carried out (see Section 4, “DFT Calculations”, for computational details). As shown briefly in Figure 5c,d, and in Figures S9–S12 (Supporting Information) in more detail, a significant change in the nature of the frontier orbital can be observed as a function of ligand. For the aliphatic hexanoic acid ligand we find that, both, occupied and empty molecular orbitals (MOs) reside over the inorganic core (Figure 5c). The introduction of the porphyrin ligand and its metalated derivatives, however, changes this significantly, and we see that the low-lying vacant orbitals are exclusively over the porphyrin moiety (Figure 5d). This shift of the $1S_e$ state onto the ligand and hence reduced exciton confinement can lead to the aforementioned reduction in PL lifetime, and a decrease in surface dipole moment (compare Figure 1). Considering the porphyrin-functionalized NCs on themselves, we see that in the case of the mZnTPP system, the occupied orbitals H, H–1, and H–2 (H = highest occupied MO or HOMO) reside almost entirely over the NC core (Figure S9, Supporting Information). However, the scenario changes once we switch to the other two porphyrin-based systems. Accordingly, even for the occupied MOs, we find significant density over the ligand for both the mMgTPP (see the H–1 and H–2 orbitals; Figure S10, Supporting Information) and the mH2TPP system (refer to the H, H–1, and H–2 orbitals; Figure S11, Supporting Information). We hypothesize that this partial extension of the occupied orbital over the ligand can contribute toward the slightly favorable optoelectronic properties of mMgTPP and mH2TPP compared to those of mZnTPP.

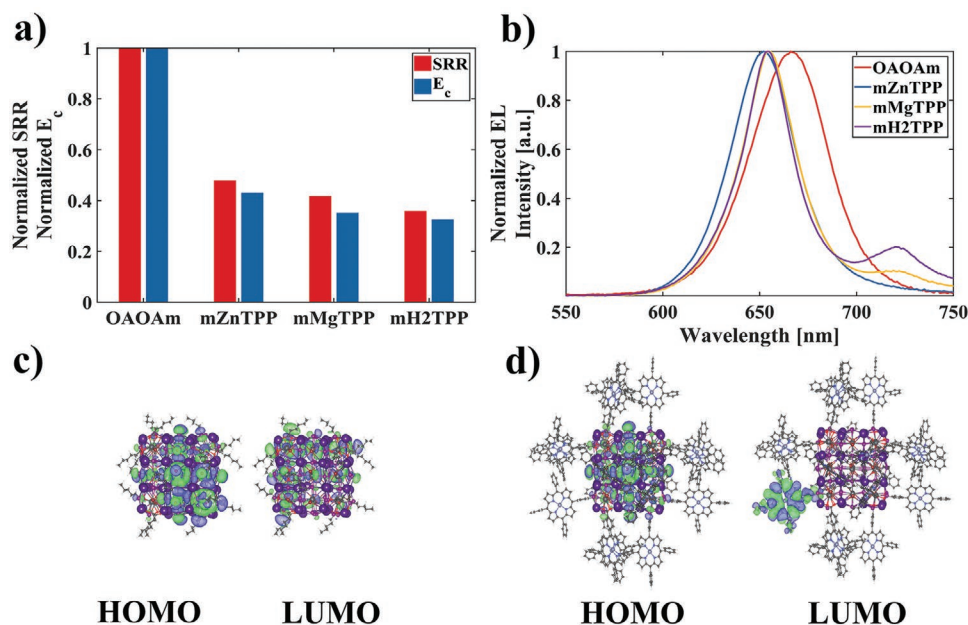


Figure 5. a) Normalized charging energy (E_c) and measured specific resistance ratios (SRR) for OAOAm and mTPP (M = Zn, Mg, H2). b) Electroluminescence spectra of devices built with differently functionalized NCs. Note that samples prepared with mMgTPP and mH2TPP exhibit parasitic emission at ≈ 725 nm. Frontier molecular orbitals of CsPbBr₂ NC decorated with c) hexanoic acid as a mimic for oleic acid and d) mZnTPP ligands.

However, we hold these high-lying, ligand-based occupied orbitals in mMgTPP and mH2TPP responsible for the parasitic emission observed near 725 nm, more so because the low-lying unoccupied orbitals, i.e., the $1S_h$ state, is always located over the ligand in the porphyrin-exchanged systems.

2.6. Optoelectronic Devices

The CsPbBr₂@SiO_x NCs with and without ligand exchange were deposited as the emitter material in the device stacks, shown in Figure 6a, with a homogeneous perovskite NC film as an emitting layer (see AFM image in Figure S13, Supporting Information). We obtained electroluminescent devices with a turn-on voltage of the current of ≈ 2.5 V (Figure 6b) and a turn-on voltage of the luminance in the range of 3–4.5 V. From this comparison, we find that the ligand exchanged NCs exhibit almost the same luminance, but at lower current densities, which results in an improved current efficacy (Figure 6c). Overall, the peak current efficacy could be enhanced by a factor of 4.65 and the necessary current density to reach the peak

Table 3. The calculated molecular polarizabilities of the different ligands in atomic units [au], OAOAm refers to the native system, mZnTPP, mMgTPP, and mH2TPP refer to the zinc, magnesium, and metal free derivative, respectively. The calculated dielectric constants as well as the charging energies (Equation (3)) are shown as well.

	Polarizability [au]	Dielectric constant	Charging energy [meV]
OAOAm	≈ 240	2.5	8.62
mZnTPP	808	4.4	4.38
mMgTPP	809	4.9	3.72
mH2TPP	797	5.1	3.49

efficacy was also lowered by approximately one order of magnitude. This could indicate that the ligand exchange leads to reduced quenching of excitons, i.e., the injected charge carriers are not lost during injection. Additionally, we find that the maximum current efficacy for the systems was located either at the onset or at higher current densities for mZnTPP and OAOAm, respectively. A possible explanation is an improved charge carrier balance in the exchanged system. We attribute both phenomena to the lower charging energy in the porphyrin-functionalized system.

3. Conclusion

To summarize, we successfully performed ligand exchange with mTPP (M = Zn, Mg, H2) derivatives on all-inorganic core-shell CsPbBr₂/SiO_x nanocrystals with a core size of 9 nm while maintaining the structural integrity of the particles. We found the optoelectronic properties of the system to be highly controllable with the nature and amount of ligand, suggesting significant electronic interaction between nanoparticle and ligand. This is also evidenced by a decrease of the first excitonic transition energy and photoluminescence lifetimes, where a dislocation of the $1S_e$ state onto the ligand could be identified as the main driving force. Additionally, the composition of the measured current, namely, the electronic and ionic contribution, was found to be dependent on the dielectric constant of the ligand. We hold a decrease of the charging energy and the manifestation of a compensating dipole moment at the NC interface responsible for the observed smaller electrical resistance. Temperature-dependent photoluminescence measurements indicated an increased phase stability of the ligand-exchanged perovskite nanocrystals. These improvements

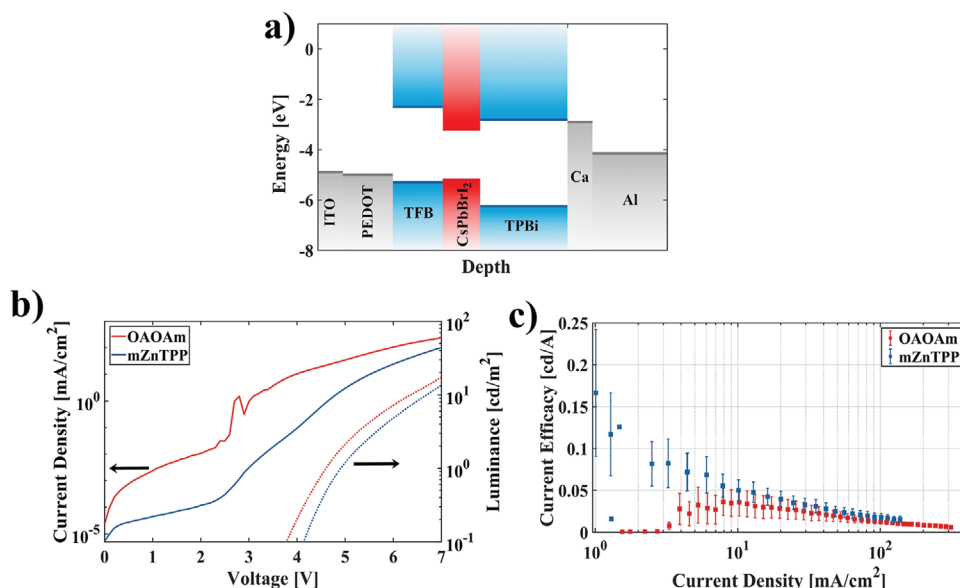


Figure 6. a) Typical stack design used for the characterization of CsPbBr₂@SiO_x NC-based light-emitting devices. b) Typical current–voltage–luminance (*j*VL) characterization curve, with the current density and luminance shown as a solid and dashed line, respectively. c) Measured current efficacies of native and exchanged perovskites in electroluminescent light-emitting devices. The efficiency curves were obtained by averaging over five different samples, each consisting of four pixels.

of the optoelectronic properties could be used to prepare light-emitting devices with enhanced current efficacy.

4. Experimental Section

Materials: 1-Octadecene (ODE), technical grade, 90%, Sigma Aldrich; OA, 97%, Acros Organics; OAm, 80–90%, Acros Organics; caesium carbonate (Cs₂CO₃), 99.99% (trace metal basis), Acros Organics; lead(II)iodide (PbI₂), 99.999% (trace metal basis), Sigma Aldrich; lead(II)bromide (PbBr₂), ≥98%, Sigma Aldrich; tetramethyl orthosilicate (TMOS), 99%, Acros Organics; toluene, HPLC grade, 99.8%; toluene, 99.8%, extra dry, AcroSeal, Acros Organics; ethyl acetate, ACS reagent, ≥99.5%, Sigma Aldrich; mZnTPP, TriPorTech; magnesium-(5-monocarboxyphenyl-10,15,20-triphenylporphyrin), 98%min, PorphyChem; (5-monocarboxyphenyl-10,15,20-triphenylporphyrin), 98%min, PorphyChem; poly(3,4-ethylenedioxythiophene) polystyrene sulfonate (PEDOT:PSS) (AI4083 or CH8000), Clevios, Heraeus Epurio; poly[(9,9-dioctylfluorenyl-2,7-diyl)-co-(4,4'-(N-(4-sec-butylphenyl)diphenylamine))] (TFB), M_w = 10 000–30 000, Lumtec; 1,3,5-tris(1-phenyl-1H-benzimidazol-2-yl)benzene (TPBi), >99.5% (HPLC), Lumtec.

Synthesis: The CsPbBr₂ nanocrystals in this work were prepared by following the literature on arrested metathesis reported by Protesescu et al. with slight modifications.^[26] In a typical synthesis, two precursors were prepared in separate flasks, one containing 203.5 mg (0.624 mmol) Cs₂CO₃ and 0.7 mL OA in 10 mL ODE. The second flask contained 116 mg (0.252 mmol) PbI₂ and 46 mg (0.125 mmol) PbBr₂ in 5 mL ODE, both flasks were dried under vacuum at 120 °C for 2 h. Immediately after the addition of OA to the first flask, gas evolution was observed due to the formation of carbonic acid which decomposes to water and carbon dioxide, ultimately indicating the formation of caesium oleate. After completion of the drying process, the flasks were set under nitrogen.

The caesium oleate flask was then heated to 150 °C to ensure completion of the caesium oleate formation, visually observable by a yellow-brownish color. Before injection, said solution was cooled to 120 °C. To dissolve the lead salts, 1 mL OA and 1 mL OAm were added to the flask, the solution was heated to 160 °C after the salts were dissolved.

Subsequently, 0.8 mL of caesium oleate precursor was quickly injected into the lead halide solution under vigorous stirring. After allowing the reaction to proceed for 5 s, the reaction was quenched by placing it in an ice-bath.

The purification was carried out via centrifugation at 4000 rpm for 12 min, the pellet was afterward redispersed in dry toluene under nitrogen atmosphere.

The general procedure for the silica shell was based upon the procedure published for CsPbBr₃ particles.^[11] The thickness of the as-synthesized shell could be tuned by using different amounts of TMOS, commonly a ratio of 5:1 (TMOS:NC) was used. A 1:1 mixture of wet and dry toluene was used as a solvent, since water is the initiator for the polymerization. After 72 h reaction time, the solution was again centrifuged at 2000 rpm for 2 min to remove unwanted larger particles and agglomerates. The supernatant was subsequently transferred to a fresh vial to obtain a stable colloidal nanoparticle dispersion. If necessary, the nanoparticle dispersion was afterwards filtered with a 200 nm syringe filter.

Ligand Exchange: The ligand exchange was carried out in solution by using a defined solution of mMTPP in toluene and adding specific volume to the NC dispersion. Upon addition, an immediate color change was observed.

The solutions, exchanged as well as native, were then used as prepared or washed with ethyl acetate (EtAc), depending on the desired analysis method. The washing step was carried out by adding 2 volumetric equivalents of EtAc to the NC dispersion followed by centrifugation. The resulting precipitate was redispersed in toluene.

Spin-Coating and Vacuum Drying: Most characterization techniques presented in this work were carried out in thin films of the as-prepared NCs. The method of choice was spin-coating under inert atmosphere. Usually, 100 μL of an ≈2 × 10⁻³ M solution (particle concentration ≈0.7 × 10⁻⁶ M) was casted onto a substrate (silica, gold, or device stack) and left at rest for 30 s. The substrate was spun at 600 rpm for 30 s with a ramp of 3 s. Because low spinning speeds were used, the spin-coater was repeatedly started 2–3 times after the initial 30 s to remove any residual solvent which remained at the edges. Subsequently, the substrate was placed in vacuum for 15 min for drying.

Conductivity Measurements: Conductivity measurements were carried out on 15 × 15 mm² silicon field-effect transistor (FET) substrates with

gold contacts of different channel lengths 2.5, 5, 10, and 20 μm obtained from the Fraunhofer IPMS, Dresden. Prior to the film preparation, the substrates were rinsed with acetone and subsequently cleaned with acetone, deionized water, and ethanol in an ultrasonic bath for 5 min each. Following the film preparation, the substrates were mounted on a custom-built sample holder under inert atmosphere which was connected to a Keithley 2634B SYSTEM SourceMeter with 10^{-9} A (nA) accuracy. Temperature-dependent conductivity measurements were carried out inside a Lake Shore Cryotronics CRX-6.5K Probe Station attached to a Keithley 2636B SYSTEM Source Meter with 10^{-12} A (pA) accuracy. In a typical film characterization, custom measurement scripts were used.

Scanning Electron Microscopy: SEM was carried out with a HITACHI SU8030 electron microscope operating with an acceleration voltage of 30 kV.

Ultraviolet Electron Spectroscopy (UPS): UPS measurements were performed using a multichamber UHV system with a base pressure of 2×10^{-10} mbar, equipped an ultraviolet source (UVS 300 SPECS) and a Phoibos 150 hemispherical photoelectron analyzer with DLD detector. Measurements were carried out with Helium I radiation (21.22 eV). The films for UPS were prepared on silicon/silicon oxide or gold substrates.

NMR Spectroscopy: NMR measurements were performed on a Bruker Avance III HDX 400, with a frequency of 400 MHz. Spectra were analyzed with the Bruker TopSpin 4.0.2 software and plotted with MatLab R2020.

UV-Vis and Photoluminescence Spectroscopy (in Solution and Solid State): Optical measurements were performed on a UV-vis-NIR spectrometer (Agilent Technologies, Cary 5000) and a fluorescence spectrometer (PerkinElmer FL8500). Both systems contain interchangeable sample holders for measurements in solution and solid state. The fluorescence spectrometer additionally provides the possibility of absolute quantum yield measurements in an integrating sphere.

Fluorescence Lifetime Measurements: The samples were excited via a picosecond pulsed laser system (EKSPLA PT400) and measured with an Acton Spectra-Pro 2300i spectrograph coupled to a Hamamatsu Streak Camera C5680 for time-resolved spectral information.

Device Characterization and Current–Voltage–Luminance (jVL) Curves: The electroluminescent devices were prepared on prestructured indium tin oxide (ITO) which was cleaned with acetone and isopropanol in an ultrasonic bath. Subsequently, a layer of PEDOT:PSS was spin-coated. On top, a layer of TFB was applied, a solution of 5 mg mL⁻¹ in chlorobenzene was spin-coated at 3000 rpm and dried at 175 °C for 30 min. The perovskite layer was prepared as described before. Above the perovskite emitters, a layer of TPBi was deposited. As a top electrode, calcium and aluminium were thermally evaporated onto the sample. The substrates were divided to four subsections, each with an active area of 2×2 mm². The devices were measured in a custom-made sample box attached to a calibrated photodiode for luminance, a two-channel Keithley 2602B source-measure unit for powering the LED and probing the electrical as well as optical output, and a JETI specbos 1211 for spectroscopic measurements. Data acquisition was carried out with a custom written LabView program.

Atomic Force Microscopy: AFM was carried out with a Bruker MultiMode 8-HR and a Bruker Dimension Icon, the obtained images were analyzed using Gwyddion.

DFT Calculations: All computations were performed using the CP2K 8.1 program suite^[27] using the PBE exchange correlation functional,^[28] MOLOPT,^[29] DZVP basis set, and GTH pseudopotentials^[30] for core electrons. A dual basis of localized Gaussians and plane waves (GPW) with a 350 Ry plane-wave cutoff was used for all calculations. Grimme's DFT-D3 protocol^[31] was used to account for van der Waals (VDW) interaction. SCF convergence criterion was set at 10^{-6} a.u. for all calculations.

Initial geometries of CsPbBr₂ nanocrystals were obtained by cutting small cubes (≈ 1.7 nm) from the bulk, exposing the CsX layer (X = Br, I) at the surface and maintaining overall charge neutrality of the particle.^[32,33] All calculations invoked a periodic boundary condition. However, to avoid spurious interaction with its periodic image, nanoparticles were placed inside a large box of size $75 \times 75 \times 75$ Å³ ensuring large vacuum

layer above the surface of the NC. All structures were then optimized in vacuum using the BFGS optimizer, setting a maximum force of 5 meV Å⁻¹ (1.0×10^{-4} hartree bohr⁻¹) as convergence criteria.

The polarizabilities of native ligands as well as the different metal-(5-monocarboxyphenyl-10,15,20-triphenylporphyrin) derivatives were carried out at the PW91/def2-TZVP level with the ORCA software.^[34] The geometries were optimized using a SCF convergence criterion of 10^{-7} .

Supporting Information

Supporting Information is available from the Wiley Online Library or from the author.

Acknowledgements

This work was supported by the DFG under grants SCHE1905/8-1, AN680/6-1, and BR1728/21-1 (Project No. 424708673) and SCHE1905/9-1. The authors would like to thank Dr. Kai Braun from the Institut für Physikalische und Theoretische Chemie, Universität Tübingen for his help with the measurements of the temperature-dependent photoluminescence spectra.

Open access funding enabled and organized by Projekt DEAL.

Conflict of Interest

The authors declare no conflict of interest.

Data Availability Statement

The data that support the findings of this study are available from the corresponding author upon reasonable request.

Keywords

electroluminescence, ligand exchange, light-emitting devices, nanocrystals, perovskites, porphyrins

Received: September 12, 2021

Revised: November 9, 2021

Published online: December 19, 2021

- [1] Y. Hassan, O. J. Ashton, J. H. Park, G. Li, N. Sakai, B. Wenger, A.-A. Haghghirad, N. K. Noel, M. H. Song, B. R. Lee, R. H. Friend, H. J. Snaith, *J. Am. Chem. Soc.* **2019**, *141*, 1269.
- [2] L. Cao, X. Liu, Y. Li, X. Li, L. Du, S. Chen, S. Zhao, C. Wang, *Front. Phys.* **2021**, *16*, 312.
- [3] A. André, M. Weber, K. M. Wurst, S. Maiti, F. Schreiber, M. Scheele, *ACS Appl. Mater. Interfaces* **2018**, *10*, 24708.
- [4] K. Kumar, J. Hiller, M. Bender, S. Nosrati, Q. Liu, M. Edelmann, S. Maier, T. Rammler, F. Wackenhut, A. J. Meixner, K. Braun, U. H. F. Bunz, M. Scheele, *ACS Nano* **2021**, *15*, 480.
- [5] P. R. Brown, D. Kim, R. R. Lunt, N. Zhao, M. G. Bawendi, J. C. Grossman, V. Bulović, *ACS Nano* **2014**, *8*, 5863.
- [6] A. Maier, D. Lapkin, N. Mukharamova, P. Frech, D. Assalauova, A. Ignatenko, R. Khubbutdinov, S. Lazarev, M. Sprung, F. Laible, R. Löffler, N. Previdi, A. Bräuer, T. Güntel, M. Fleischer, F. Schreiber, I. A. Vartanyants, M. Scheele, *Adv. Mater.* **2020**, *32*, 2002254.

- [7] F. Krieg, Q. K. Ong, M. Burian, G. Rainò, D. Naumenko, H. Amenitsch, A. Süess, M. J. Grotevent, F. Krumeich, M. I. Bodnarchuk, I. Shorubalko, F. Stellacci, M. V. Kovalenko, *J. Am. Chem. Soc.* **2019**, *141*, 19839.
- [8] M. Scheele, W. Brütting, F. Schreiber, *Phys. Chem. Chem. Phys.* **2015**, *17*, 97.
- [9] X. Feng, Y. Huan, C. Zheng, C. Tan, H. Meng, B. Liu, D. Gao, W. Huang, *Org. Electron.* **2020**, *77*, 105522.
- [10] K. Gkini, N. Balis, M. Papadakis, A. Verykios, M.-C. Skoulikidou, C. Drivas, S. Kennou, M. Golomb, A. Walsh, A. G. Coutsolelos, M. Vasilopoulou, P. Falaras, *ACS Appl. Energy Mater.* **2020**, *3*, 7353.
- [11] F. Zhang, Z.-F. Shi, Z.-Z. Ma, Y. Li, S. Li, D. Wu, T.-T. Xu, X.-J. Li, C.-X. Shan, G.-T. Du, *Nanoscale* **2018**, *10*, 20131.
- [12] R. Grisorio, M. E. Di Clemente, E. Fanizza, I. Allegretta, D. Altamura, M. Striccoli, R. Terzano, C. Giannini, M. Irimia-Vladu, G. P. Suranna, *Nanoscale* **2019**, *11*, 986.
- [13] B. Fritzing, R. K. Capek, K. Lambert, J. C. Martins, Z. Hens, *J. Am. Chem. Soc.* **2010**, *132*, 10195.
- [14] P. Hui, *Chin. Phys. Lett.* **2004**, *21*, 160.
- [15] K. Zheng, Q. Zhu, M. Abdellah, M. E. Messing, W. Zhang, A. Generalov, Y. Niu, L. Ribaud, S. E. Canton, T. Pullerits, *J. Phys. Chem. Lett.* **2015**, *6*, 2969.
- [16] A. Harriman, *J. Chem. Soc., Faraday Trans. 1* **1980**, *76*, 1978.
- [17] J. Karolczak, D. Kowalska, A. Lukaszewicz, A. Maciejewski, R. P. Steer, *J. Phys. Chem. A* **2004**, *108*, 4570.
- [18] J.-P. Strachan, S. Gentemann, J. Seth, W. A. Kalsbeck, J. S. Lindsey, D. Holten, D. F. Bocian, *J. Am. Chem. Soc.* **1997**, *119*, 11191.
- [19] Y.-C. Zhao, W.-K. Zhou, X. Zhou, K.-H. Liu, D.-P. Yu, Q. Zhao, *Light: Sci. Appl.* **2017**, *6*, e16243.
- [20] A. Senocrate, J. Maier, *J. Am. Chem. Soc.* **2019**, *141*, 8382.
- [21] J. Yi, X. Ge, E. Liu, T. Cai, C. Zhao, S. Wen, H. Sanabria, O. Chen, A. M. Rao, J. Gao, *Nanoscale Adv.* **2020**, *2*, 4390.
- [22] B. Tang, L. J. Ruan, C. Qin, A. Shu, H. He, Y. Ma, *Adv. Opt. Mater.* **2020**, *8*, 2000498.
- [23] F. Bertolotti, L. Protesescu, M. V. Kovalenko, S. Yakunin, A. Cervellino, S. J. L. Billinge, M. W. Terban, J. S. Pedersen, N. Masciocchi, A. Guagliardi, *ACS Nano* **2017**, *11*, 3819.
- [24] P. Cottingham, R. L. Brutchey, *Chem. Commun.* **2016**, *52*, 5246.
- [25] A. J. Quinn, P. Beecher, D. Iacopino, L. Floyd, G. de Marzi, E. V. Shevchenko, H. Weller, G. Redmond, *Small* **2005**, *1*, 613.
- [26] L. Protesescu, S. Yakunin, M. I. Bodnarchuk, F. Krieg, R. Caputo, C. H. Hendon, R. X. Yang, A. Walsh, M. V. Kovalenko, *Nano Lett.* **2015**, *15*, 3692.
- [27] T. D. Kühne, M. Iannuzzi, M. D. Ben, V. V. Rybkin, P. Seewald, F. Stein, T. Laino, R. Z. Khaliullin, O. Schütt, F. Schiffrmann, D. Golze, J. Wilhelm, S. Chulkov, M. H. Bani-Hashemian, V. Weber, U. Borštnik, M. Tallefumier, A. S. Jakobovits, A. Lazzaro, H. Pabst, T. Müller, R. Schade, M. Guidon, S. Andermatt, N. Holmberg, G. K. Schenter, A. Hehn, A. Bussy, F. Belleflamme, G. Tabacchi, A. Glöß, I. B. M. Lass, C. J. Mundy, C. Plessl, M. Watkins, J. VandeVondele, M. Krack, J. Hutter, *J. Chem. Phys.* **2020**, *152*, 194103.
- [28] J. P. Perdew, K. Burke, M. Ernzerhof, *Phys. Rev. Lett.* **1996**, *77*, 3865.
- [29] J. VandeVondele, J. Hutter, *J. Chem. Phys.* **2007**, *127*, 114105.
- [30] M. Krack, *Theor. Chem. Acc.* **2005**, *114*, 145.
- [31] G. Lippert, J. Hutter, M. Parrinello, *Mol. Phys.* **1997**, *92*, 477.
- [32] S. Grimme, J. Antony, S. Ehrlich, H. Krieg, *J. Chem. Phys.* **2010**, *132*, 154104.
- [33] S. ten Brinck, I. Infante, *ACS Energy Lett.* **2016**, *1*, 1266.
- [34] F. Neese, *WIREs Comput. Mol. Sci.* **2012**, *2*, 73.